

Time-resolved surface acoustic wave propagation across a single grain boundary

D. H. Hurley

Idaho National Laboratory, Idaho Falls, Idaho 83415-2209, USA

O. B. Wright, O. Matsuda, T. Suzuki, and S. Tamura

Department of Applied Physics, Graduate School of Engineering, Hokkaido University, Sapporo 060-8628, Japan

Y. Sugawara

School of Physics and Astronomy, University of Southampton, Southampton SO17 1BJ, United Kingdom

(Received 4 October 2005; revised manuscript received 11 January 2006; published 7 March 2006)

Using an optical technique, we present time-resolved measurements of high frequency surface acoustic waves propagating across the boundary between two single crystals. The choice of the elastically anisotropic cubic crystal copper allows the observation of anisotropic surface acoustic propagation with cuspidal wave fronts together with refraction in the presence of significant orientation mismatch. The effect of the subsurface grain boundary angle on the transmitted acoustic field is revealed.

DOI: [10.1103/PhysRevB.73.125403](https://doi.org/10.1103/PhysRevB.73.125403)

PACS number(s): 62.65.+k, 63.20.Dj, 68.35.Iv, 68.35.Ja

I. INTRODUCTION

The propagation of sound across discontinuities in solids is of vital importance in acoustics. Subjects as diverse as acoustic insulation, earthquake dynamics, medical acoustics, and nondestructive testing rely on a detailed knowledge of the transmission and reflection of acoustic waves at interfaces. For bulk acoustic interaction between media of general anisotropy, the acoustic Fresnel equations can be applied to calculate the reflected and refracted acoustic amplitudes.¹ At frequencies for which continuum approximations are valid, these established equations underpin acoustics in inhomogeneous materials, allowing, for example, the prediction of the effects of microstructure on sound propagation in polycrystals.²

In the case of surface acoustic waves (SAWs), closed form solutions for acoustic propagation between orientationally mismatched crystallites are not available for general orientations, and the problem is compounded by the extra degrees of freedom introduced by the angles between the normal to the crystallite-crystallite interface and that to the free surface.³ This problem is important in the prediction of SAW propagation on polycrystalline materials involving wavelengths as large as the order of a kilometer or greater in seismology,⁴ or as small as the order of one micron in ultrasonic nondestructive testing.^{5–8} It is also important in the burgeoning field of SAW devices.⁹ However, the three-dimensional geometry involved in the experimental study of such SAW scattering has greatly limited the amount of research done. The most promising route to experimentation on length scales accessible in the laboratory is to fully characterize the SAW field by acoustic imaging techniques. Qualitative imaging studies of SAW reflection and refraction at grain boundaries in polycrystalline LiNbO_3 using scanning electron microscopy¹⁰ and in granular rocks using laser acoustics¹¹ have been reported. Related quantitative studies of twist-bonded crystals by bulk phonon imaging¹² and of single dislocations by x-ray stroboscopic SAW imaging¹³ have also been published, but to date no quantitative studies

involving the real time imaging of SAWs at a single crystalline interface seem to have been made. Using a real-time optical generation and detection technique for SAWs,^{14,15} we present here a quantitative study of the transmission of SAWs across a boundary between misoriented grains of the highly elastically anisotropic metal copper (fcc structure).

II. EXPERIMENTAL METHOD

We make use of an ultrafast optical pump and probe technique with a common-path Sagnac interferometer for detection.^{14–16} A brief description is as follows: Pump optical pulses of duration ~ 1 ps, wavelength 415 nm, pulse energy ~ 1.0 nJ, and repetition rate 80 MHz are focused at 60° incidence through a system of cylindrical lenses and a microscope objective to circular spot of diameter $D \sim 4$ μm [see Fig. 1(a)]. A transient temperature distribution (up to ~ 200 K rise) thermoelastically excites the surface acoustic wave packets with frequencies in the 100 MHz to 1 GHz range. Out-of-plane (z -directed) surface motion (≤ 100 pm $= 1$ \AA) is detected with ~ 0.3 pm resolution by two probe optical pulses separated by 300 ps. These are focused at normal incidence onto the (optically isotropic) copper surface through another microscope objective to a spot size $D/2 \sim 2$ μm , and the difference in phase between these two pulses, proportional to the velocity of the surface motion, is detected. The position of the probe spot is scanned laterally (with $\sim 100 \times 100$ pixels taking ~ 7 min per image) at a fixed pump-probe delay time, and this delay is then varied in steps of 1.25 ns to produce a 12.5 ns animation of 10 frames with a lateral spatial resolution $\sim D$. The high purity (5 N) polycrystalline copper sample is polished to a mirror finish and etched in a dilute mixture of hydrochloric and hydrofluoric acids. The crystal orientation is mapped by microscopy based on electron backscatter diffraction:¹⁷ Figure 1(b) shows such a map for a $0.85 \text{ mm} \times 0.69 \text{ mm}$ region. We study the boundary between two grains marked A and B in

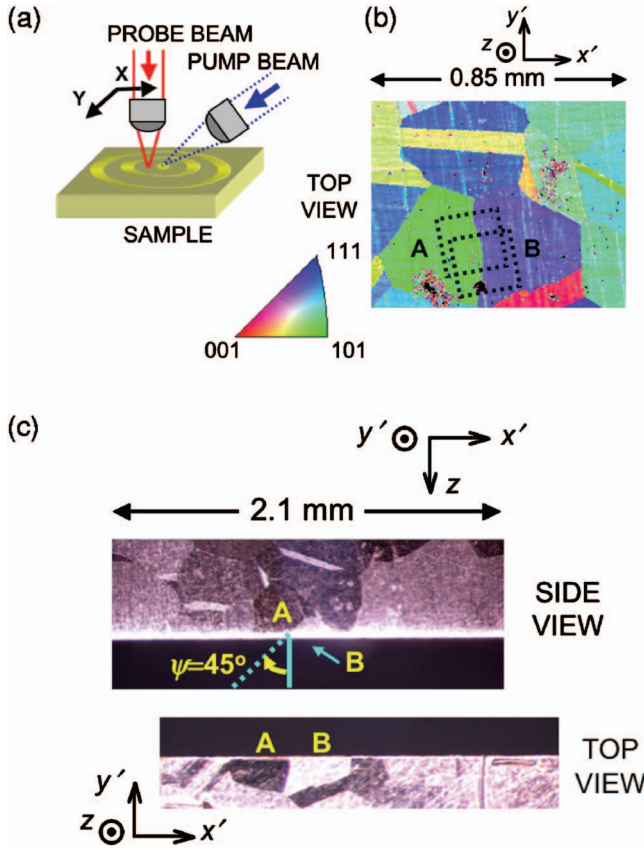


FIG. 1. (Color) (a) Schematic experimental arrangement. (b) Crystal orientation image of the polycrystalline copper sample showing the probed regions (dotted lines). The grains marked A and B correspond to the $(8\ 1\ 10)$ and $(\bar{8}\ 11\ \bar{6})$ surfaces, respectively. (c) Optical micrographs of the sample after sectioning, showing the subsurface orientation of the grain boundary and the definition of the subsurface angle ψ between the grains (side view). The top view of the sample is also shown. The side view has been rotated so that the top surface is facing down for ease of comparison with the top view. The horizontal and vertical axes (x' and y') in (b) and (c) are inclined with respect to the axes (x and y) used for imaging.

Fig. 1(b), corresponding, respectively, to the $(8\ 1\ 10)$ and $(\bar{8}\ 11\ \bar{6})$ surfaces.¹⁸

III. REAL-TIME EXPERIMENTAL DATA

Figures 2(a) and 2(b) show two consecutive experimental SAW images corresponding to the excitation of grain A at an interval of 6.25 ns over a $200\ \mu\text{m} \times 200\ \mu\text{m}$ region, identified by the upper dotted square in Fig. 1(b). Figure 2(d) is a map of the probe beam reflectivity for the same region, showing the position of the grain boundary. Figures 3(a)–3(d) show corresponding images for the excitation of grain B over the region identified by the lower dotted square in Fig. 1(b). Figures 4 and 5 show 10 consecutive frames spaced by 1.25 ns, corresponding to the excitation of grains A and B, respectively.¹⁹ The multiple wave fronts arise because of the periodic laser excitation. The surface acoustic wave packets have a central wavelength $\sim 10\ \mu\text{m}$ (deter-

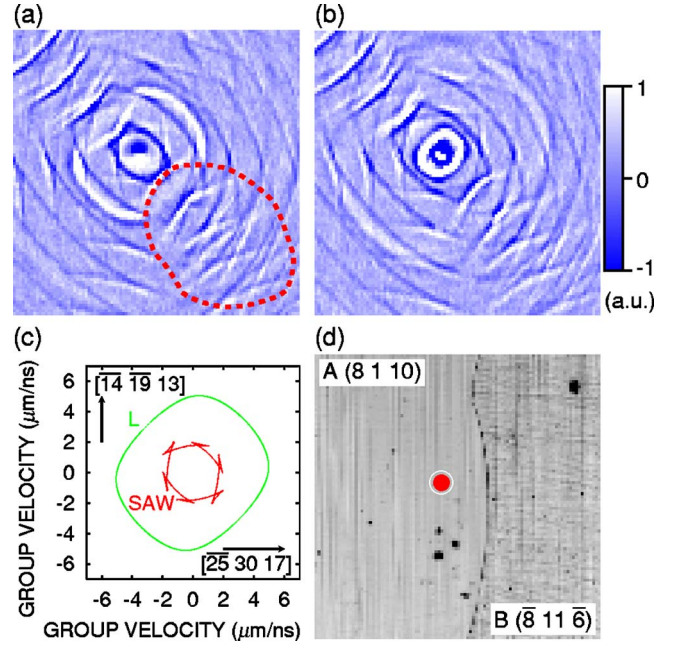


FIG. 2. (Color online) (a) and (b) Experimental SAW images corresponding to the excitation of grain A at an interval of 6.25 ns over a $200\ \mu\text{m} \times 200\ \mu\text{m}$ region. The lighter regions in the gray-scale region (white-blue online) correspond to a surface velocity that is directed out-of-plane. The dashed region in (a) indicates an example of where refraction effects are easily visible. (c) Group velocity surfaces for grain A. (d) Probe beam reflectivity for the same region, showing the grain boundary and excitation point (as the small ring).

mined mainly by the value of D and by thermal diffusion), corresponding to an acoustic pulse duration ~ 3 ns. Because of the relatively broad frequency spectrum (100 MHz–1 GHz), the enhancement of the intensity in the caustic directions is limited.

The anisotropy factor, $A = 2c_{44}/(c_{11} - c_{12})$, for pure Cu is 3.2 (see Ref. 20), leading to folded group velocity surfaces for the SAWs and to cuspidal wave fronts (also referred to as phonon focusing). Moreover, one expects noticeable SAW refraction effects at mismatched grain boundaries as well as mode conversion. As a first step to understand the data quantitatively, we solve the relevant secular equation for the acoustic angular dispersion (subject to the appropriate boundary conditions):^{1,20}

$$|l_i l_n c_{ijnm} - \delta_{jm} \rho v^2| = 0, \quad (1)$$

where c_{ijkl} , ρ , v , and l_i are, respectively, defined as the elastic stiffness tensor, the density, the acoustic phase velocity and the dimensionless wave vectors. The calculated group velocity surfaces, or wave front patterns, for SAWs, pseudo-SAWs (PSAWs-existing for grain B only) and bulk quasilongitudinal waves (L) that propagate close to the surface are shown in Figs. 2(c) and 3(c) for the $(8\ 1\ 10)$ and $(\bar{8}\ 11\ \bar{6})$ surfaces, respectively. These bulk quasilongitudinal waves can also be termed surface skimming bulk waves. For propagation in directions of high symmetry away from a thermoelastic line source, for example, they form part of a wave front that turns

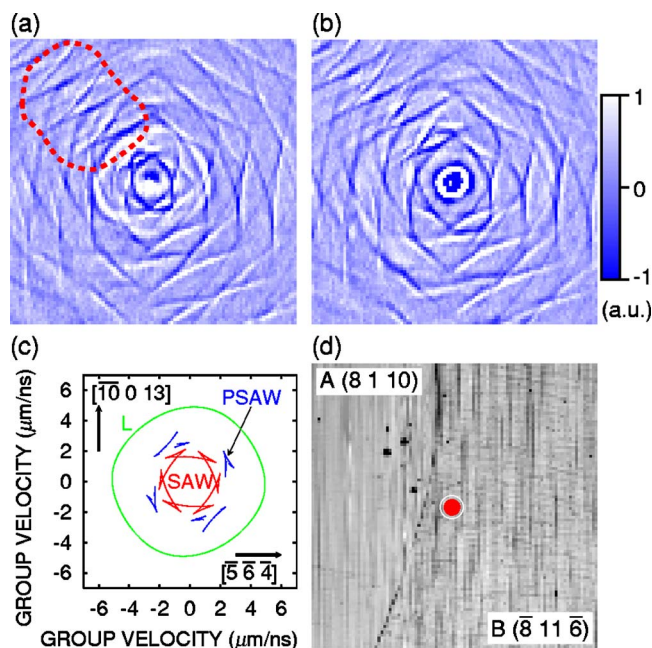


FIG. 3. (Color online) (a) and (b) Two experimental SAW images corresponding to the excitation of grain B at an interval of 6.25 ns over a $200\ \mu\text{m} \times 200\ \mu\text{m}$ region. The dashed region in (a) indicates an example of where refraction effects are easily visible. (c) Group velocity surfaces for grain B. (d) Probe beam reflectivity for the same region, showing the grain boundary and excitation point (as the small ring).

on at a point determined by the bulk longitudinal velocity and turns off at a point determined by the bulk shear velocity.²¹

The calculated wave front pattern for SAWs excited on the $(8\ 1\ 10)$ surface (grain A) shows a symmetry similar to that expected for a $(1\ 0\ 1)$ surface.²² Over an angle of 360° there are a total of 12 cusps in the wave front. In the grain A side of the image the calculated SAW wave front corre-

sponds closely to the data, suggesting that the effect of any acoustic reflection from the grain boundary does not have a major impact on the displacement field in this region. For certain directions between cusps, three closely spaced SAW wave fronts are predicted. However, these cannot be clearly distinguished in the data because of the finite SAW pulse width. The L wave front forms a distinct ring in the images that is evident, for example, as the small white ring near the center of Fig. 2(b). Indeed, for an ideal elastic solid the L wave exhibits sharp features in the surface elastodynamic Green's function, as shown by Every *et al.*^{23,24} The observed attenuation of the L wave front is larger than that of the SAW. This is expected from the intrinsic coupling of the L wave front to bulk quasishear modes. [Both SAW and L wave fronts suffer geometrical attenuation associated with a point source: for an isotropic solid, for example, the amplitude of circular surface wave fronts go down with distance as $1/\sqrt{r}$ (see Ref. 22).] No PSAW modes can exist for this crystal cut. (PSAWs behave like SAWs, with a higher phase velocity than SAWs for a given direction in an anisotropic solid, but differ in being intrinsically leaky modes.²⁰) The calculated fast and slow bulk quasitransverse modes are omitted because no evidence for them are seen in the data (probably because of the relatively symmetric geometry of excitation and the out-of-plane motion detection.)

The calculated wave front pattern for SAWs excited on the $(\bar{8}\ 11\ \bar{6})$ surface (grain B—see Fig. 3) exhibits approximately sixfold symmetry, similar to that expected for a $(1\ 1\ 1)$ surface,²² and this pattern again corresponds closely to the data because of the absence of significant acoustic reflection. As before, 12 cusps appear in the wave front over 360° . PSAW wave fronts, also shown in Fig. 3(c), are not easily distinguished among the SAWs in the images, although we demonstrate their existence below. The calculated L wave front again corresponds well with the smooth shape observed, and, as before, no evidence for quasitransverse modes is seen.

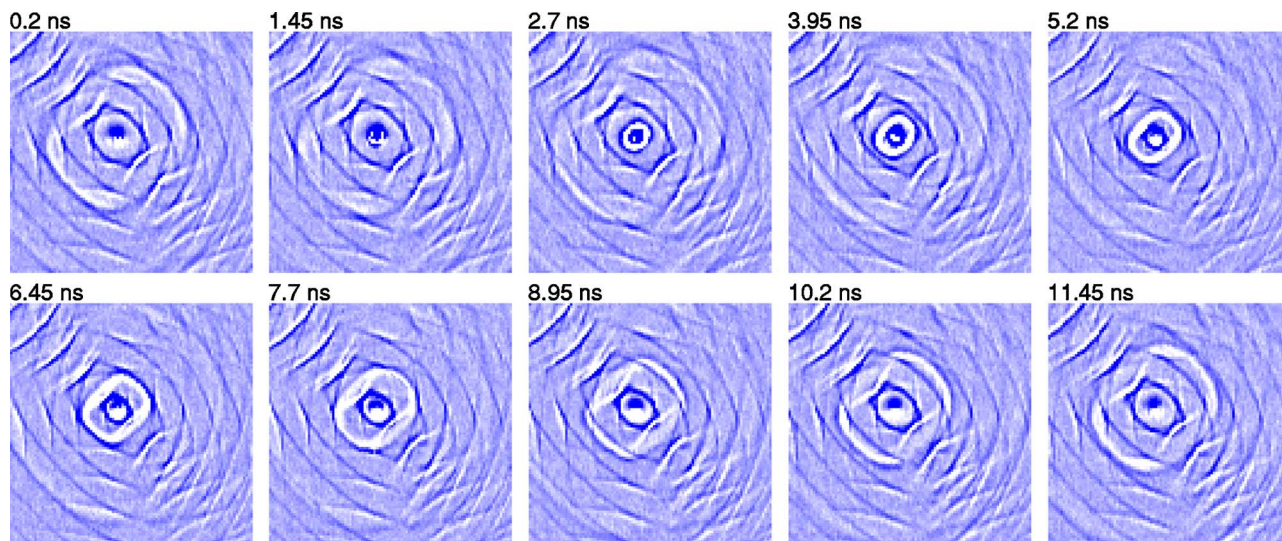


FIG. 4. (Color online) A series of experimental SAW images corresponding to the excitation of grain A at intervals of 1.25 ns over a $200\ \mu\text{m} \times 200\ \mu\text{m}$ region. The 10.2 and 3.95 ns images correspond to Figs. 2(a) and 2(b).

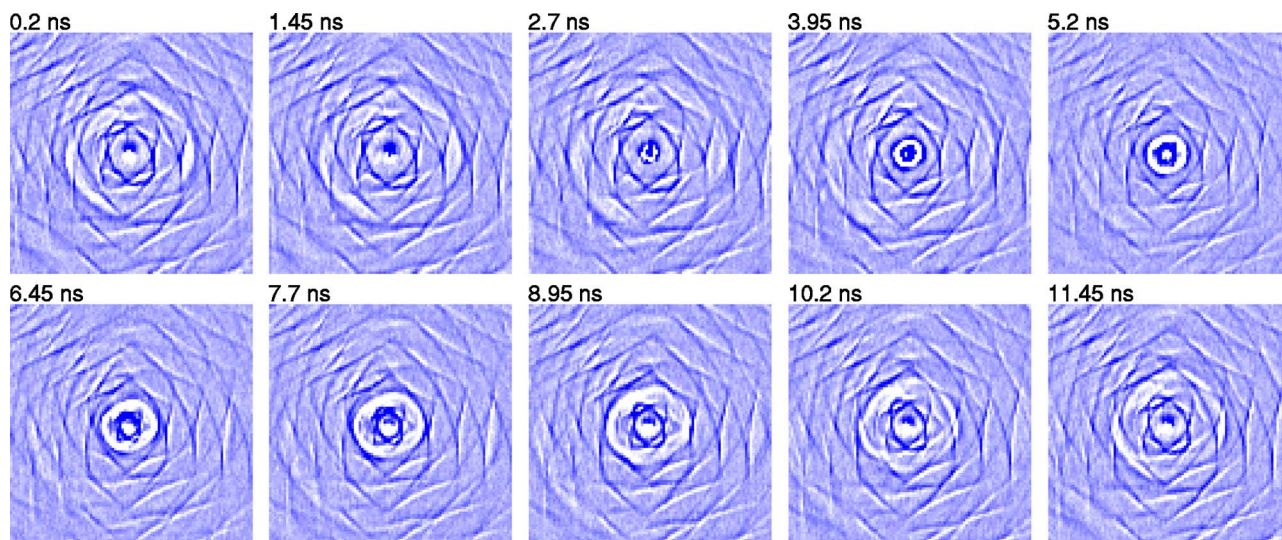


FIG. 5. (Color online) A series of experimental SAW images corresponding to the excitation of grain B at intervals of 1.25 ns over a $200\ \mu\text{m} \times 200\ \mu\text{m}$ region. The 10.2 and 3.95 ns images correspond to Figs. 3(a) and 3(b).

IV. FOURIER TRANSFORMS OF DATA AND NUMERICAL SIMULATIONS

Compared to the group velocity surface, the slowness surface (or, equivalently, the constant frequency surface) is more directly related to elastic properties. The slowness surface is accessible from the image data by taking a combination of temporal and dual spatial Fourier transforms of the complete animations corresponding to Figs. 4 and 5 (see Ref. 25). The results are shown in Figs. 6(a) and 6(b) for a frequency of 240 MHz. In contrast to the real time data for the wave fronts, the experimental slowness surfaces have the advantage of not containing overlapping contributions due to the laser repetition rate. The corresponding calculated slowness surfaces at this frequency for grains A and B alone are shown in Figs. 6(c) and 6(d), respectively. Because of the near-central position of the excitation spot and (vertical) grain boundary in the images, the shape of the experimental slowness surfaces are strongly influenced by grain A for negatively directed wave vectors k_x (where x is the horizontal axis) and by grain B for positively directed k_x . For grain B excitation it is evident that PSAWs are also present because of the appearance of their characteristic branches for $k_x > 0$. Unlike the real space images, the slowness surfaces show unambiguously the modes excited for each wave vector direction.

The experimental SAW wave fronts show intricate refraction effects, visible for example in the dashed regions in Figs. 2(a) and 3(a). In contrast to the case of a plane wave crossing the boundary, the concentration effect arising from cuspidal wave fronts enhances the surface displacement in certain directions, and it is in these directions of higher amplitude that the refraction effects are more easily discerned. (In the past this enhancement has been dramatically revealed, for example, by sprinkling dust on the surface of crystals.²⁶) Mode conversion at the boundary may also be occurring, but we could not detect any clear evidence for this in the images. For quantitative analysis one should consider the acoustic

generation and subsequent transmission across the grain boundary. Thermoelastic surface wave generation on arbitrarily orientated crystalline surfaces is a complex process;^{21,27} although the thermal expansion tensor of copper is isotropic, the elastic constant tensor is not, resulting in an anisotropic acoustic source. However, for the purposes of simplified numerical modeling,^{14,28} we approximate the generation by an initial surface-normal displacement $u=u(r=|r|, t=0)$ with a hemispherical Gaussian spatial variation,

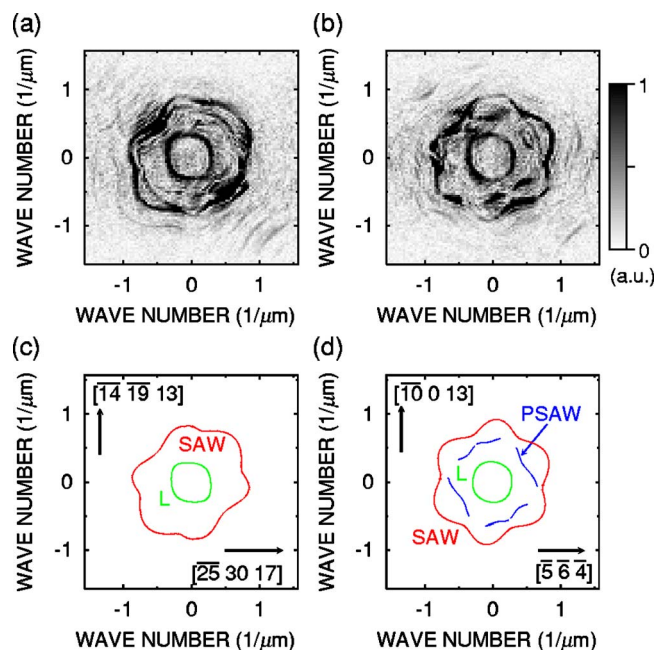


FIG. 6. (Color online) (a) and (b) Experimental slowness surfaces obtained from the combined temporal and dual spatial Fourier transform of the animations for the A-B grain system when exciting grains A and B, respectively. The gray scale corresponds to the intensity of the modes excited. (c) and (d): Calculated slowness surfaces for grains A and B alone, respectively.

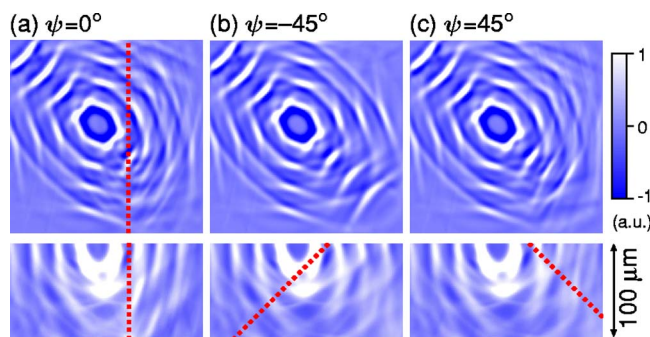


FIG. 7. (Color online) (a)–(c) FDTD simulation images of the outward surface velocity of the surface regions of the copper sample probed when grain A is excited, corresponding to the data of Fig. 2(a), for three different subsurface grain boundary angles ψ . The experimentally determined angle is $\psi=45^\circ$. Lower plots: z -component of the displacement for sections through a horizontal center line.

$u \propto e^{-r^2/R^2}$ where $R=5 \mu\text{m}$, repeated at intervals of 12.5 ns. Figures 7(a)–7(c) and Figs. 8(a)–8(c) show the results of the predicted surface velocity for such a numerical calculation over a $200 \mu\text{m} \times 200 \mu\text{m}$ region with excitation in grains A and B, respectively, using the FDTD (finite difference time domain) method²⁹ for three different representative subsurface grain boundary angles: $\psi=0^\circ$ and $\pm 45^\circ$. A planar A-B grain boundary is assumed, and is chosen close to the actual boundary location. The angle ψ , defined in Fig. 1(c), was experimentally determined by sectioning the sample (along the line approximately bisecting the two grains) after the SAW imaging measurements were complete. Optical micrographs of this cut, shown in Fig. 1(c), demonstrate that the present sample corresponds to $\psi=45 \pm 5^\circ$. (The side view has been rotated so that the top surface faces down for ease of comparison with the top view.)

Comparing the predictions of the FDTD simulations for different ψ with the two sets of data, it is difficult to ascertain which corresponds most closely to the experimental data. Both angles $\psi=45^\circ$ and -45° appear to give fair agreement with the observed form of the transmitted (refracted) wave fronts. Several details of the observed wave fronts differ from the predictions: The characteristic shapes of the quasi-longitudinal bulk waves observed in experiment are not reproduced in the simulations. The exact form of the transmitted wave fronts is also somewhat different. These discrepancies are likely to be due to our approximate treatment of the acoustic source, but other effects, such as an imperfect interface between the grains, may play some role. The predicted subsurface z -directed displacement fields corresponding to the different ψ are also shown, revealing energy channelling to the bulk; the complexity of the three-dimensional transient elastic fields associated with the acoustic transmission across the grain boundary is evident. Qualitatively, one might expect the $\psi=0^\circ$ geometry to show the closest analogy

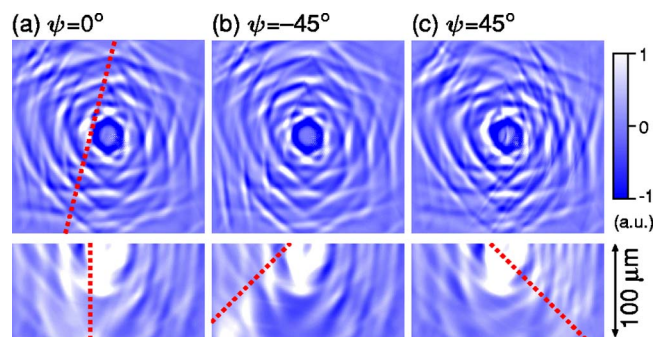


FIG. 8. (Color online) (a)–(c) FDTD simulation images of the outward surface velocity of the surface regions of the copper sample probed when grain B is excited, corresponding to the data of Fig. 3(a), for three different subsurface grain boundary angles ψ . The experimentally determined angle is $\psi=45^\circ$. Lower plots: z -component of the displacement for sections through a horizontal center line.

to the problem of normally incident bulk waves on a plane boundary. A tilted subsurface boundary should effect the reflection and transmission coefficients, as well as being likely to enhance mode conversion by redirecting energy in the direction perpendicular to the surface. Unfortunately our limited data do not allow us to pursue this problem further. A series of samples with different ψ should be prepared for this purpose, and excitation with plane waves rather than with point-excited waves would greatly simplify the analysis. A further improvement would be the use of a laser with a lower repetition rate or the use of a pulse picker in order to eliminate the complicating effects of overlapping wave fronts. Moreover, further simulations with a more accurate representation of the acoustic source are necessary to better understand the experimental wave fields.

V. CONCLUSIONS

There are eight independent degrees of freedom in the geometry of SAW transmission between two crystalline grains: these correspond to 2 (Euler) angles to define the crystal plane of grain A at the A-B interface, 2 angles to define the corresponding crystal plane of grain B, one angle to define the relative rotation of grains A and B about the normal to the interface, 2 angles to define the orientation of the surface, and one angle to define the angle of acoustic incidence.³⁰ We have only investigated a tiny subset of such angles for the case of a copper-copper interface. This work, therefore, suggests a wide range of further investigations into the interaction of SAWs with interfaces in anisotropic media that should have ramifications in many fields. Moreover, the extension using near-field optical techniques to higher SAW frequencies should allow the probing of disorder, strain or Kapitza resistance at the boundary between grains with relevance to material fracture and thermal transport.³¹

- ¹B. A. Auld, in *Acoustic Fields in Solids*, 2nd ed. (Krieger, Malabar, 1990), Vols. I and II.
- ²E. P. Papadakis, *J. Acoust. Soc. Am.* **37**, 703 (1965).
- ³P. Malischewsky, *Surface Waves and Discontinuities* (Elsevier, Amsterdam, 1987).
- ⁴M. P. Barmin, M. H. Ritzwoller, and A. L. Levshin, *Pure Appl. Geophys.* **158**, 1351 (2001).
- ⁵A. Aharoni, M. Tur, and K. M. Jassby, *Appl. Phys. Lett.* **59**, 3530 (1991).
- ⁶H. Willems and K. Goebbels, *Met. Sci.* **15**, 549 (1981).
- ⁷W. M. Gao, C. Glorieux, S. E. Kruger, K. Van de Rostyne, V. Gusev, W. Lauriks, and J. Thoen, *Mater. Sci. Eng., A* **313**, 170 (2001).
- ⁸D. H. Hurley, K. L. Telschow, and D. Cottle, *Ultrasonics* **40**, 617 (2002).
- ⁹T. Uemura, S. Fujii, H. Kitabayashi, K. Itakura, A. Hachigo, H. Nakahata, S. Shikata, K. Ishibashi, and T. Imai, *Jpn. J. Appl. Phys., Part 1* **41**, 3476 (2002).
- ¹⁰D. Roshchupkin and M. Brunel, *IEEE Trans. Ultrason. Ferroelectr. Freq. Control* **41**, 512 (1994).
- ¹¹J. A. Scales and A. E. Malcolm, *Phys. Rev. E* **67**, 046618 (2003).
- ¹²M. Msall, W. Dietsche, K. J. Friedland, and Q. Y. Tong, *Phys. Rev. Lett.* **85**, 598 (2000).
- ¹³D. Shilo and E. Zolotoyabko, *Phys. Rev. Lett.* **91**, 115506 (2003).
- ¹⁴Y. Sugawara, O. B. Wright, O. Matsuda, M. Takigahira, Y. Tanaka, S. Tamura, and V. E. Gusev, *Phys. Rev. Lett.* **88**, 185504 (2002).
- ¹⁵Y. Sugawara, O. B. Wright, and O. Matsuda, *Rev. Sci. Instrum.* **74**, 519 (2003).
- ¹⁶D. H. Hurley and O. B. Wright, *Opt. Lett.* **24**, 1305 (1999).
- ¹⁷*Electron Backscatter Diffraction in Materials Science*, edited by A. J. Schwarz, M. Kumar, and B. L. Adams (Kluwer Academic, New York, 2000).
- ¹⁸The raw Miller indices were multiplied by a common factor and rounded with a round-off error $<5\%$.
- ¹⁹See <http://kino-ap.eng.hokudai.ac.jp> for animations of this data and also for animations of the theoretical simulations. Alternatively, see EPAPS Document No. E-PRBMDO-73-040612 (<http://ftp.aip.org/cgi-bin/epaps?ID=E-PRBMDO-73-040612>) for the animations. For more information on EPAPS, see <http://www.aip.org/pubserve/epaps.html>.
- ²⁰G. W. Farnell, in *Physical Acoustics*, edited by W. P. Mason and R. N. Thurston (Academic, New York, 1970), Vol. 6, p. 109. The elastic constants are taken as $c_{11}=168.4$ GPa, $c_{12}=121.4$ GPa, $c_{44}=75.2$ GPa, and the density as $\rho=8.93$ g cm $^{-3}$.
- ²¹D. H. Hurley and J. B. Spicer, *J. Acoust. Soc. Am.* **116**, 2914 (2004).
- ²²R. E. Camley and A. A. Maradudin, *Phys. Rev. B* **27**, 1959 (1983).
- ²³A. G. Every and G. A. D. Briggs, *Phys. Rev. B* **58**, 1601 (1998).
- ²⁴X. Zhang, J. D. Comins, A. G. Every, P. R. Stoddart, W. Pang, and T. E. Derry, *Phys. Rev. B* **58**, 13677 (1998).
- ²⁵Y. Sugawara, O. B. Wright, and O. Matsuda, *Appl. Phys. Lett.* **83**, 1340 (2003).
- ²⁶A. A. Kolomenskii and A. A. Maznev, *Phys. Rev. B* **48**, 14502 (1993).
- ²⁷A. G. Every, K. Y. Kim, and A. A. Maznev, *J. Acoust. Soc. Am.* **102**, 1346 (1997).
- ²⁸D. H. Hurley and K. L. Telschow, *Phys. Rev. B* **71**, 241410(R) (2005).
- ²⁹See A. Tavlove, *The Finite-Difference Time-Domain Method* (Artech House, Boston, 1998). The grid size used is $\delta x=\delta y=\delta z=0.5$ μ m and $\delta t=20$ ps.
- ³⁰An exception applies to transversely isotropic materials, for which there are 6 degrees of freedom.
- ³¹E. T. Swartz and R. O. Pohl, *Rev. Mod. Phys.* **61**, 605 (1989).